nature electronics

Review article

https://doi.org/10.1038/s41928-024-01167-3

Van der Waals opto-spintronics

Received: 23 August 2023

Accepted: 16 April 2024

Published online: 22 May 2024

Check for updates

J. Tyler Gish [1], Dmitry Lebedev [1], Thomas W. Song[1], Vinod K. Sangwan [1] & Mark C. Hersam [1,2,3]

Van der Waals materials with long-range magnetic order show a range of correlated phenomena that could be of use in the development of optoelectronic and spintronic applications. Magnetically ordered van der Waals semiconductors with spin-polarized currents are, in particular, sensitive to external stimuli such as strain, electrostatic fields, magnetic fields and electromagnetic radiation. Their combination of two-dimensional magnetic order, semiconducting band structure and weak dielectric screening means that these materials could be used to create novel atomically thin opto-spintronic devices. Here we explore the development of van der Waals opto-spintronics. We examine the interplay between optical, magnetic and electronic excitations in van der Waals magnetic semiconductors, and explore the control of their magnetization via external stimuli. We consider fabrication and passivation strategies for the practical handling and design of opto-spintronic devices. We also explore potential opto-spintronic device architectures and applications, which include magnonics, quantum transduction, neuromorphic computing and non-volatile memory.

By exploiting spin instead of charge as a state variable, spintronics could provide a lower-energy pathway for information processing and storage compared with conventional digital electronics. In one of the earliest spintronic discoveries, it was found that multilayer ferromagnetic (FM) films are less resistive when all the spins are aligned due to spin-dependent scattering[1,2]. This is the basis of giant magnetoresistance read heads in commercial magnetic memory storage and has led to a range of low-power spintronic technologies[3].

Alongside developments in spintronics, the past two decades have seen rapid advances in two-dimensional (2D) van der Waals (vdW) materials and devices. The earliest works focused on graphene and included efforts to fabricate transistors for ultrafast digital computing[4]. However, the absence of a semiconducting bandgap in graphene limits field-effect current modulation and undermines its utility in information processing. The subsequent discovery of vdW semiconductors with a bandgap—such as 2D transition metal dichalcogenides (TMDCs)—has led to the development of high-performance transistors and also optoelectronic devices such as photodetectors, light-emitting diodes (LEDs) and solar cells[5]. Furthermore, the recent discovery of layered vdW materials with unpaired spins and long-range magnetic order down to the atomically thin limit[6–8] has resulted in the design and fabrication of atomically thin spintronic devices for low-power and non-volatile memory applications[9,10].

Two-dimensional materials can concurrently host both optoelectronic and spintronic phenomena and can be used to create opto-spintronic devices. Such devices have a range of potential applications, including neuromorphic computing and ultrafast terahertz systems that exploit optically addressable spin–orbit interactions at picosecond timescales[11]. As disparate 2D materials can be used to form vdW heterostructures, one route to 2D opto-spintronics is to stack different vdW materials. The heterostructures can be engineered using materials with varying optoelectronic and magnetic properties, coupled together by proximity effects, orbital overlap and/or hybridization[12,13]. Another approach is to rely on spin-polarized magnetic vdW semiconductors where weak dielectric screening enables enhanced electrostatic control compared with bulk materials. For example, the vdW magnetic semiconductor CrI_3 in a tunnelling geometry has been used to create a photodetector that is sensitive to the helicity of circularly polarized light[14–16] (Fig. 1).

In this Review, we explore light–matter interactions in vdW magnetic materials and examine the control of magnetization in vdW

[1]Department of Materials Science and Engineering, Northwestern University, Evanston, IL, USA. [2]Department of Chemistry, Northwestern University, Evanston, IL, USA. [3]Department of Electrical and Computer Engineering, Northwestern University, Evanston, IL, USA. e-mail: m-hersam@northwestern.edu

https://doi.org/10.1038/s41928-024-01167-3

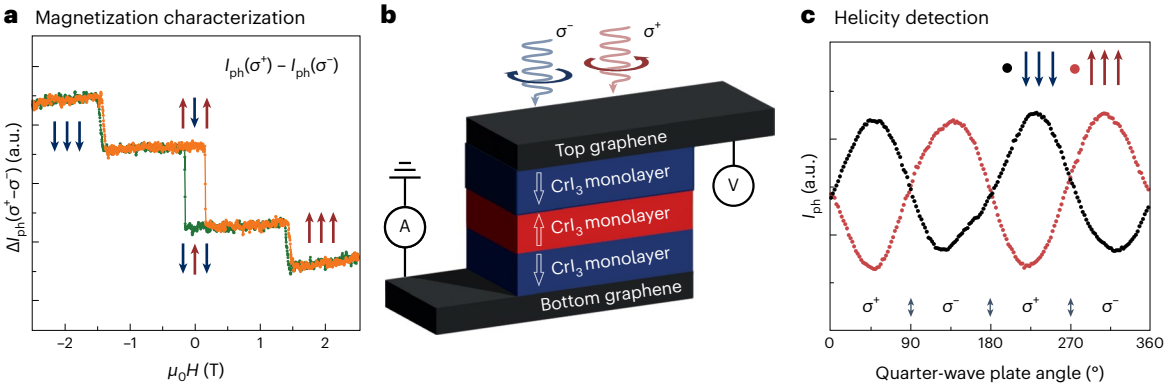

Fig. 1 | CrI_3 tunnelling devices for light helicity detection. a, Differential photocurrent, ΔI_{ph}, for right-handed (σ^-) versus left-handed (σ^+) circularly polarized light, showing the spin-flip transitions in trilayer CrI_3 as a function of applied magnetic field ($\mu_0 H$; blue and red arrows illustrate the spin alignment of the three vdW layers of CrI_3)[14]. **b**, A schematic of a CrI_3 vertical tunnelling device exposed to circularly polarized light. **c**, Helicity dependence can be observed in the photocurrent versus quarter-wave plate angle data[14]. Panels adapted with permission from: **a**,**c**, ref.14, AAAS, under a Creative Commons licence CC BY-NC 4.0.

magnets via external stimuli (such as pressure, electrostatic gating and light). We then consider the practical challenges of fabricating and characterizing semiconducting devices based on vdW magnets. Finally, we discuss potential opto-spintronic device architectures and applications.

Light–matter interactions in vdW magnets

Magneto-optical methods, such as the magneto-optical Kerr effect (MOKE) and magnetic circular dichroism (MCD), are commonly used to detect magnetization in 2D magnetic materials. For example, these methods were used for the first confirmation of 2D FM ordering in atomically thin CrI_3, which showed thickness-dependent magnetization due to antiferromagnetic (AFM) stacking of FM layers (A-type AFM) in few-layer CrI_3 (ref. 7). However, MOKE and MCD are challenging to apply to materials with no net magnetization such as materials with fully compensated AFM order[17]. By contrast, linear dichroism (LD) relies on the differential absorption of linearly polarized light and is sensitive to materials with optical anisotropy (such as zigzag or non-collinear AFM)[18,19]. In particular, a large LD signal was observed down to monolayer $FePS_3$ due to the presence of in-plane optical anisotropy[19]. AFM ordering can also be probed optically with second harmonic generation (SHG), which occurs via magnetic dipole interactions in centrosymmetric materials or electric dipole interactions in non-centrosymmetric materials[17]. In centrosymmetric and A-type AFM CrI_3, magnetic order breaks both spatial-inversion and time-reversal symmetries, and gives rise to an SHG signal down to bilayer thickness. There is no observable signal in monolayer CrI_3 due to FM ordering and insufficient magnetic dipole contributions[20]. However, the SHG signal for monolayer CrSBr, which is FM and centrosymmetric, is detectable due to magnetic dipole contributions[21]. Magnetic materials that are ferroelectrically polarized (multiferroic materials) see an enhancement of the SHG signal due to electric dipole contributions. NiI_2 is an example of a recently discovered 2D multiferroic material where helical AFM order induces spontaneous electrical polarization. Observable LD and SHG signals serve as the primary evidence in support of NiI_2 as the first monolayer multiferroic material, which is further supported by theoretical modelling[22,23].

Light–matter interactions, beyond magneto-optical effects, occur because of the formation of excitons in 2D semiconductors. In materials with long-range magnetic order, excitons may couple with the spin-polarized band structure, resulting in correlated phenomena (Box 1). For example, in CrI_3, the absorption of linearly polarized light gives rise to several excitonic features[24]. The phonon-mediated relaxation from these excited states results in circularly polarized photoluminescence (PL) in monolayer CrI_3, originating from the coupling to the FM order. The PL helicity depends on the net magnetization of the crystal, which can switch directions upon field-induced flipping of the magnetization direction (Box 1, exciton polarization)[25]. Although similar effects have also been observed in vdW FM $CrBr_3$, recent theoretical work points to different origins of the coupling between excitons and the underlying magnetic order in this case[26]. The size and energy of the excitons also depend on the interlayer electronic coupling, which can be manipulated in magnetic systems (Box 1, exciton confinement). In particular, in A-type AFM CrSBr, the exciton is confined to a single FM layer. However, a spin-flip transition from AFM to FM order results in exciton delocalization across two layers, lowering the PL energy by 20 meV, which provides a means for magnetic-field manipulation of electronic transitions[27]. Furthermore, a recent theoretical report predicts electrical-field switching between FM and AFM states in bilayer CrSBr, thus providing another opportunity for exciton energy tuning[28].

Strong coupling of excitons with magnetic order in materials that host many-body quantum-entangled ground states has recently been observed in $NiPS_3$ and NiI_2 (refs. 29,30). In $NiPS_3$, the excitonic transition couples with zigzag AFM order, resulting in an ultranarrow PL peak with a linewidth of 0.4 meV (Box 1, many-body excitons), which originates from the quantum-entangled ground-state interactions between the spin-polarized electron on Ni and a hole sitting on the S ligands[29]. An analogous excitonic transition was also observed in the AFM helimagnet NiI_2, probably originating from coupling to the non-collinear magnetic structure of NiI_2 and its ferroelectric order. The strong spin–charge coupling resulting from the multiferroic order changes the parity conditions of the excitonic transition when compared with $NiPS_3$, resulting in a dark process that is detectable through only optical absorption spectroscopy[30].

Polarons result from the coupling of optically excited charges or excitons with lattice vibrations (phonons). For instance, the local symmetry breaking and lattice distortions at ultrafast timescales result in the formation of photoexcited polarons in CrI_3 (ref. 31). Other optically excited polarons in CrI_3 emerge from the coupling between excitonic transitions and longitudinal phonon modes that persist down to bilayer thickness. In particular, polarization-dependent Raman studies reveal an increase of electron–photon coupling by 50% upon the emergence of magnetic order in CrI_3. The field-induced AFM-to-FM transition also tunes the intensity of polaron modes, suggesting strong coupling between lattice, charge and spin degrees of freedom in 2D CrI_3 (ref. 24). In $NiPS_3$, LD measurements reveal strong coupling between the many-body excitonic transition and out-of-plane vibrational phonon

https://doi.org/10.1038/s41928-024-01167-3

BOX 1

Excitons in van der Waals magnets

Exciton polarization. The spin-polarized band structure can lead to the formation of optically excited states with spin-polarized charge carriers. Depending on the magnetic ordering and selection rules, exciton recombination can produce circularly polarized luminescence, with handedness corresponding to the magnetization direction. This effect has been observed in CrI_3 with out-of-plane magnetization, where luminescence is circularly polarized[25].

Exciton confinement. The magnetic structure can modify the electronic coupling between layers, affecting the spatial confinement of excitons. Changing the magnetic structure via external stimuli (such as magnetic field, strain) thus enables tuning of the exciton energy. This effect has been observed in bilayer crystals of CrSBr, which show AFM order but can be converted to FM via a spin-flip transition, resulting in delocalization of the exciton from one to two layers[27].

Many-body excitons. Quantum-entangled ground states in magnetic systems can give rise to many-body excitonic transitions, which are coupled to the underlying magnetic order. In some cases, these excitons coexist with the formation of an electrical dipole. These many-body excitonic transitions yield ultranarrow luminescence linewidths on the order of millielectronvolts and a high degree of linear polarization, $\rho=(I_{\parallel}-I_{\perp})(I_{\parallel}+I_{\perp})$, as has been observed in $NiPS_3$ (ref. 29).

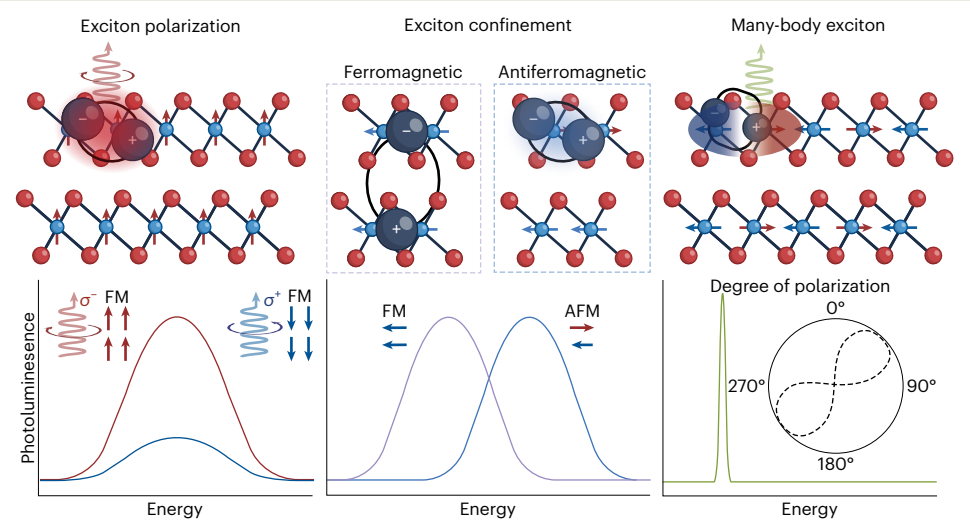

Various excitonic effects in a magnetically ordered vdW material, characterized by photoluminescence. For simplicity, the structure reflects a prototypical bilayer magnetic vdW system, with the blue circles corresponding to spin-polarized metal centres and the red circles corresponding to a ligand environment.

modes. Over ten exciton–phonon bound states are correlated with the ultranarrow excitonic peak. This coupling between the excitonic transition and the out-of-plane vibrational mode leads to the stretching and contracting of the S–Ni bonds, which modifies the ligand-field charge transfer and ultimately the electronic structure of the crystal[18]. Ultrafast spectroscopy has also been used to probe the phonon modes in the same spectral region of $NiPS_3$, although this work assigns them to localized *d*–*d* transitions with coupling between *d* orbitals and phonons[32]. These localized *d*–*d* transitions are attributed to the breaking of local inversion symmetry following the formation of long-range magnetic order. The ultrafast timescales of these phonon-mediated processes potentially enable ultrafast opto-spintronic devices.

In addition to coupling to phonons, optically excited charge carriers or excitons in magnetically ordered materials can couple with collective spin waves (magnons). For example, CrI_3 hosts two magnon branches with in-phase (acoustic, lower energy) or out-of-phase (optical, higher energy) spin precession that can be optically driven[33]. In monolayer CrI_3, the in-phase acoustic magnon is correlated with the helicity of the exciting circularly polarized optical irradiation. As the helicity corresponds to the magnetic-ordering direction, this effect can be controlled using an external magnetic field[34].

The coupling of optically excited phonons with electronic structure has also been probed in zigzag AFM $FePS_3$ (Fig. 2a), which can hybridize with a magnon mode[35]. In particular, pump–probe measurements have revealed an optically excited phonon mode at 3.2 THz that correlates with the *d*–*d* electronic transitions (Fig. 2c,d). This in-plane vibrational mode of $FePS_3$ couples orthogonally to the zigzag AFM magnetic structure (Fig. 2b). Moreover, by applying an external magnetic field, the 3.2 THz phonon mode hybridizes with a magnon at 3.6 THz, forming a strongly coupled phonon–magnon branch whose frequency can be tuned with an external magnetic field[35]. This work demonstrates the ability to optically launch coherent phonons with intensities correlated to electronic transitions and field-tunable phonon–magnon coupling. The coupling of excitonic transition with magnons has been observed in semiconducting AFM CrSBr (Fig. 2e). Optical pumping CrSBr with photon energies above the bandgap creates excitons and simultaneously launches coherent magnons. Optical probing of the magnons micrometres away from the pump location reveals strong hybridization between excitons and magnons that is tunable with an external magnetic field[36,37] (Fig. 2f–h), thus enabling the launching of coherent magnons correlated with the exciting optical irradiation.

https://doi.org/10.1038/s41928-024-01167-3

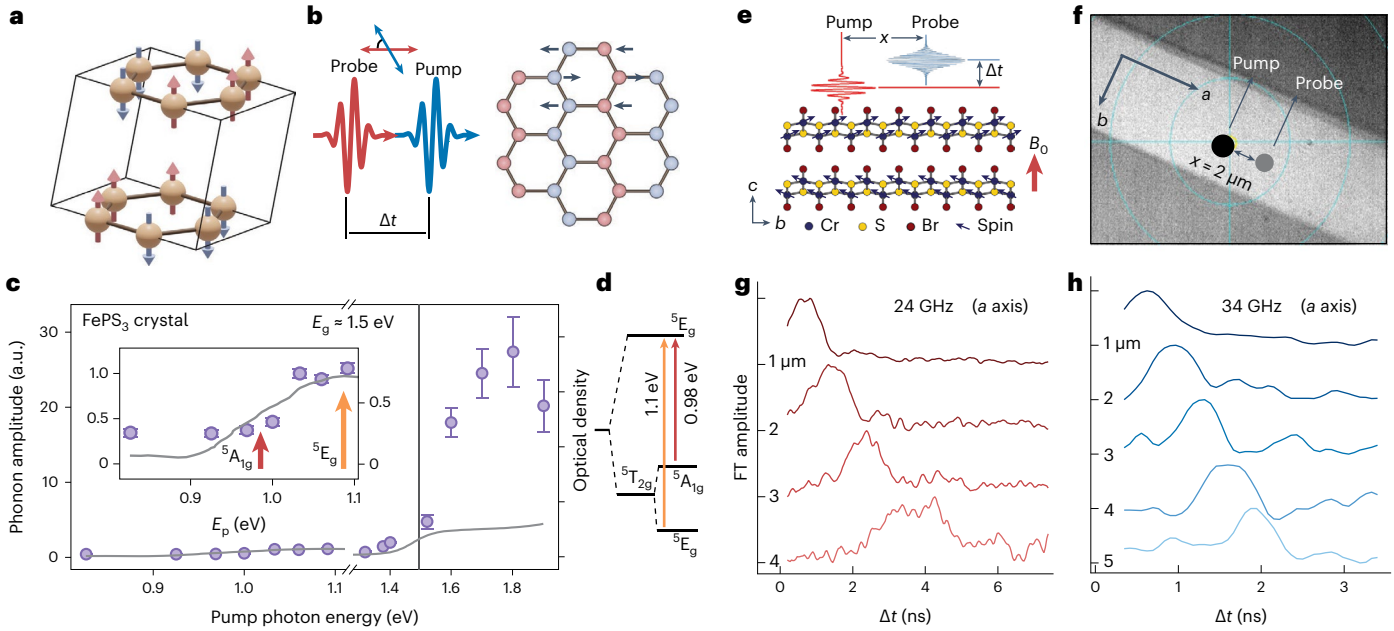

Fig. 2 | Optically excited phonons and magnons in vdW magnetic semiconductors. a, A unit cell of $FePS_3$ showing the Fe ions and the corresponding zigzag AFM order (blue and red arrows indicate antiparallel spin alignment). **b**, A schematic of a time-resolved pump and probe experiment where the pump and probe light pulses are delayed by time Δt, with the blue and red lines indicating the difference in linear polarization between the pulses (45° for $FePS_3$). The black arrows on the $FePS_3$ honeycomb lattice illustrate the optically active phonon mode[35]. **c**, Amplitude of the 3.2 THz signal on a bulk $FePS_3$ crystal at 10 K as a function of pump photon energy (E_p). The grey curve shows the optical absorption spectrum. The inset shows a zoomed-in plot to better illustrate the correlation with the *d*–*d* transitions. The vertical line at 1.5 eV marks the bandgap, E_g (ref. 35). **d**, A schematic of the *d*–*d* electronic transitions split by the octahedral and trigonal ligand fields.[35] **e**, Detection of magnon spin waves in CrSBr using a spatially separated pump and probe technique. A canting magnetic field B_0 = 0.2 T is applied normal to the 2D planes[36]. **f**, An optical image of bulk CrSBr showing the spatial separation, *x*, of the pump and probe pulse. The probe pulse is delayed by Δt in time and spatially offset by distance *x*. **g**,**h**, Probe-wavelength integrated short-time Fourier transform (FT) spectra at different probe distances along the *a* axis for the 24 GHz and 34 GHz magnon modes, respectively[36]. Panels adapted with permission from: **a**–**d**, ref. 35, under a Creative Commons licence CC BY 4.0; **e**–**h**, ref. 36, Springer Nature Ltd.

External control of magnetic order

Manipulating magnetic properties via external stimuli such as electrostatic gating or strain is useful for spintronic applications such as memory and low-power computing devices. One of the earliest examples of electrostatic control of magnetism in vdW materials involved bilayer CrI_3, where a dual gating structure (Fig. 3a) enabled independent control of carrier concentration and applied electric field. Magneto-electric coupling results from the coupling between magnetic (electrical) polarization and external electric (magnetic) fields. For example, in AFM bilayer CrI_3, applying an out-of-plane electric field causes spins to flip across the interface resulting in a constant magnetization that increases with increasing electric field[38]. Charge modulation can also tune the magnetic order. In bilayer CrI_3, hole doping increases the coercive field, while electron doping decreases it (Fig. 3b) to the point that the layers became magnetically decoupled[39]. In addition, a change of the magnetic order can be achieved through carrier doping by applying a magnetic field and then varying the charge density[38,39]. Electrostatic control of magnetism has been demonstrated in $CrGeTe_3$ using an ionic liquid gate, resulting in increased magnetocrystalline anisotropy that raises the FM ordering temperature from 61 K to 200 K (ref. 40).

Magnetic order depends on exchange interactions, which are dictated by the crystal structure of the material. The 2D nature of layered vdW materials results in a small energy difference between stacking polytypes. Each polytype has a unique topology of exchange interactions. Therefore, changing the stacking order can allow tuning of the magnetic structure in 2D materials[41]. For example, applying hydrostatic pressure induces an AFM-to-FM transition in bilayer CrI_3 (refs. 42,43). While the pressure tuning in CrI_3 is irreversible due to the monoclinic-to-rhombohedral transition[42], reversible AFM-to-FM transitions have been demonstrated in CrSBr by applying tensile strain. Strain applied along the *a* axis exceeding a critical value of 1.3% results in a redshift of the PL. This redshifting corresponds to an AFM-to-FM magnetic transition (Fig. 3c,d) and is a result of strain-induced modulation of the lattice constant that alters the exchange interactions[44].

Light–matter interactions in magnetic materials can also modify electronic interactions and, consequently, magnetic order. For instance, all-optical magnetic switching is observed in CrI_3 due to its strong optical absorption and large excitonic and magneto-optical responses. The all-optical magnetic switching in this case is maximized with a circularly polarized laser pulse, which has been attributed to angular momentum transfer rather than thermal or inverse Faraday effect processes[45] (Fig. 3e,f). Moreover, pump–probe measurements using circularly polarized light allow the demagnetization of CrI_3 to be studied at ultrafast timescales down to 100 fs, which originates from coherent coupling between the magnetization and out-of-plane vibrational phonon mode. These results demonstrate that strong spin–phonon coupling in CrI_3 enables control over vibrational and magnetic dynamics via photon helicity[46]. Optical manipulation of magnetization has also been explored in $NiPS_3$ (refs. 47,48). Specifically, optical excitation of the in-plane magnon mode shows a strong correlation with the AFM order in $NiPS_3$, which is sensitive to the polarization of light. The amplitude of the coherent magnon oscillations is correlated with the Néel vector direction due to ultrafast modification of the magnetocrystalline anisotropy induced by the laser pulse[47]. Ultrafast spectroscopy studies on the magnetic excitons in $NiPS_3$ further reveal the emergence of itinerant conductivity due to dissociation of the excitonic state into mobile carriers, subsequently launching coherent magnon oscillations. This generation of free carriers persists for several picoseconds, maintaining the long-range magnetic order[48].

https://doi.org/10.1038/s41928-024-01167-3

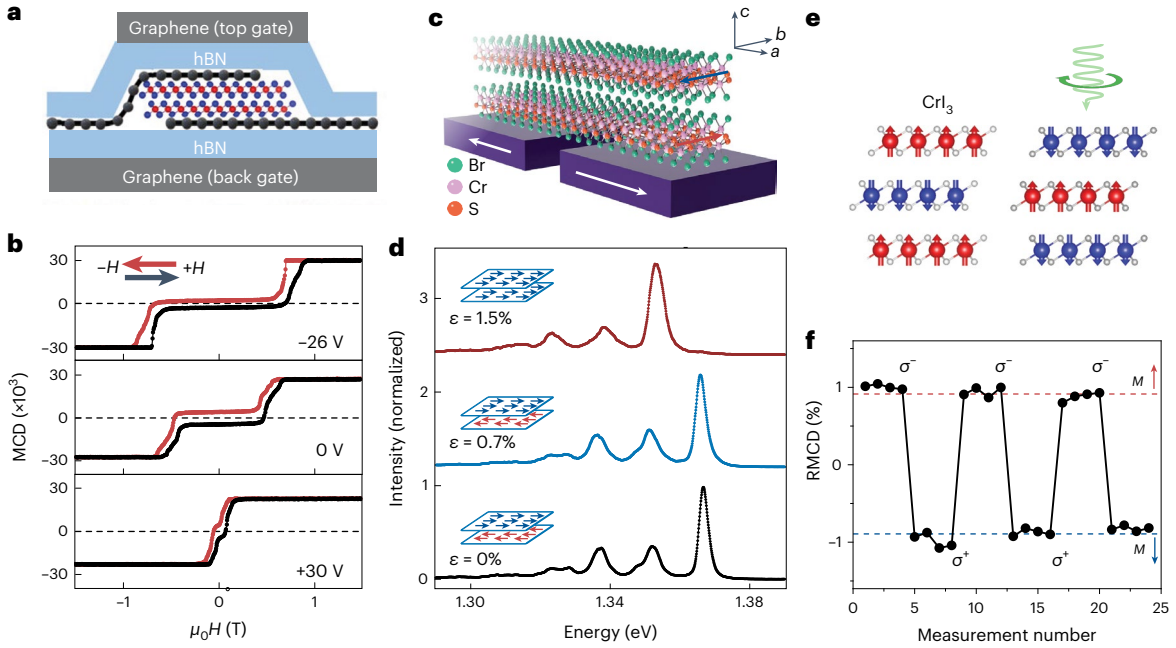

Fig. 3 | External stimuli control of the magnetization in vdW magnets. **a**, Side-view schematic of a dual-gated bilayer CrI_3 field-effect device. The atoms sandwiched between hBN correspond to carbon (grey, that is, single-layer graphene) and chromium/iodine (red/blue) in CrI_3 (ref. 39). **b**, MCD of the device shown in **a** at 4 K. The spin-flip transition decreases monotonically as the electron doping increases by tuning the gate voltage from negative to positive, leading to a near collapse of the AFM ground state[39]. **c**, Uniaxial strain measurement set-up up used to measure CrSBr on a SiO_2/Si substrate with a gap on the order of micrometres[44]. **d**, Selected PL spectra showing the transition from AFM to FM with increasing strain ε (ref. 44). **e**, AFM-coupled CrI_3 layers showing the optical switching of magnetization using a circularly polarized laser pulse (green arrow)[45]. **f**, Reflectance magneto-circular dichroism (RMCD) demonstrating controllable switching between two magnetization states ($M\uparrow$ and $M\downarrow$) via pulsed polarized light without any external magnetic field[45]. Panels adapted with permission from: **a**,**b**, ref. 39, Springer Nature Ltd; **c**,**d**, ref. 44, Springer Nature Ltd; **e**,**f**, ref. 45, Springer Nature Ltd.

Fabrication and characterization

The strong light–matter interactions in 2D magnetic materials also enable opportunities to study and utilize these materials in electronic devices. However, the high chemical reactivity of many 2D magnetic materials requires that additional care is needed in materials handling and device fabrication to achieve stable charge transport in a manner that preserves electronic and magnetic structure. In addition, accessing high-quality, few-layer 2D magnetic crystals often requires more advanced methods than traditional scotch-tape exfoliation. One such method directly evaporates alumina onto the magnetic material (such as Fe_3GeTe_2), followed by mechanical cleavage, resulting in few-layer Fe_3GeTe_2 that is otherwise challenging to isolate[49] (Fig. 4a). A related technique uses exfoliation on Ti/Au (less than 3 nm thick) substrates, resulting in monolayer crystals up to a few millimetres in lateral dimensions. As the Ti/Au thin film is highly resistive, local back-gated monolayer field-effect transistors (FETs) can be directly fabricated without the need to etch the underlying metallic thin film[50]. Another common issue with 2D magnetic materials is that few-layer flakes are often in direct proximity to substantially thicker neighbouring regions that complicate device fabrication. In this case, targeted flake removal using a viscoelastic stamp enables selective removal of the thicker areas, resulting in isolated few-layer flakes (Fig. 4b). This use of targeted flake removal has enabled the fabrication of high-quality few-layer NiI_2 FETs, which have been used to electrically probe the multiferroic transition temperature down to monolayer thicknesses[51].

Many 2D magnetic materials are highly reactive with poor stability in ambient conditions, which introduces challenges for device fabrication, characterization and integration. For example, although CrSBr and $NiPS_3$ are relatively air-stable in bulk form, exfoliated flakes degrade in ambient conditions within a few days to weeks[29,52–55]. Other vdW magnetic materials such as NiI_2, $CrBr_3$, CrI_3 and $CrGeTe_3$ are considerably less stable with irreversible and catastrophic degradation occurring within seconds to hours[6,8,51,56]. Therefore, encapsulation methods are critical for fundamental studies and device applications of many 2D magnetic materials. In particular, the most common encapsulation strategy uses a dry-transfer process that caps the sensitive material on both sides with a chemically stable and electronically inert vdW material (such as hexagonal boron nitride (hBN); Fig. 4c). While encapsulation with hBN flakes is sufficient for interim handling between an air-free chamber and subsequent measurements, it is insufficient for long-term stability due to diffusion of reactive atmospheric species to the interior of the encapsulated structure from the flake edges[56,57]. Therefore, for the most reactive 2D magnetic materials, atomic layer deposition (ALD) of metal-oxide layers are employed either as a primary encapsulation or as a secondary encapsulation in addition to hBN. To promote uniform ALD growth and prevent direct reaction of ALD precursors with chemically sensitive 2D magnetic materials, organic ALD seeding layers[58,59] are often utilized, resulting in months of ambient stability even for the most reactive 2D transition metal halides such as CrI_3 (ref. 57; Fig. 4d).

Another limiting factor in studying vdW magnetic semiconductors is their high electrical resistivity. For example, although CrI_3 has measurable n-type charge transport at room temperature (field-effect mobility of around 0.001 $cm^2 V^{-1} s^{-1}$ and on/off ratio of around 10^3), CrI_3 is insulating at low temperatures where it shows magnetic ordering, thus limiting device architectures to tunnelling geometries[57,60]. Nevertheless, A-type AFM ordering of CrI_3 results in a large tunnelling magnetoresistance on the order of 10,000% (refs. 60,61). The magnetic ordering in the tunnelling barrier has also been exploited in ambipolar spin tunnel FETs[62]. Fortunately, not all vdW magnetic materials are insulating at low temperatures, which enables lateral charge transport measurements below the magnetic-ordering temperature. For example, CrSBr shows measurable semiconducting charge transport down to temperatures as low as 5 K (ref. 52). In this manner, lateral charge transport measurements enable electrical

https://doi.org/10.1038/s41928-024-01167-3

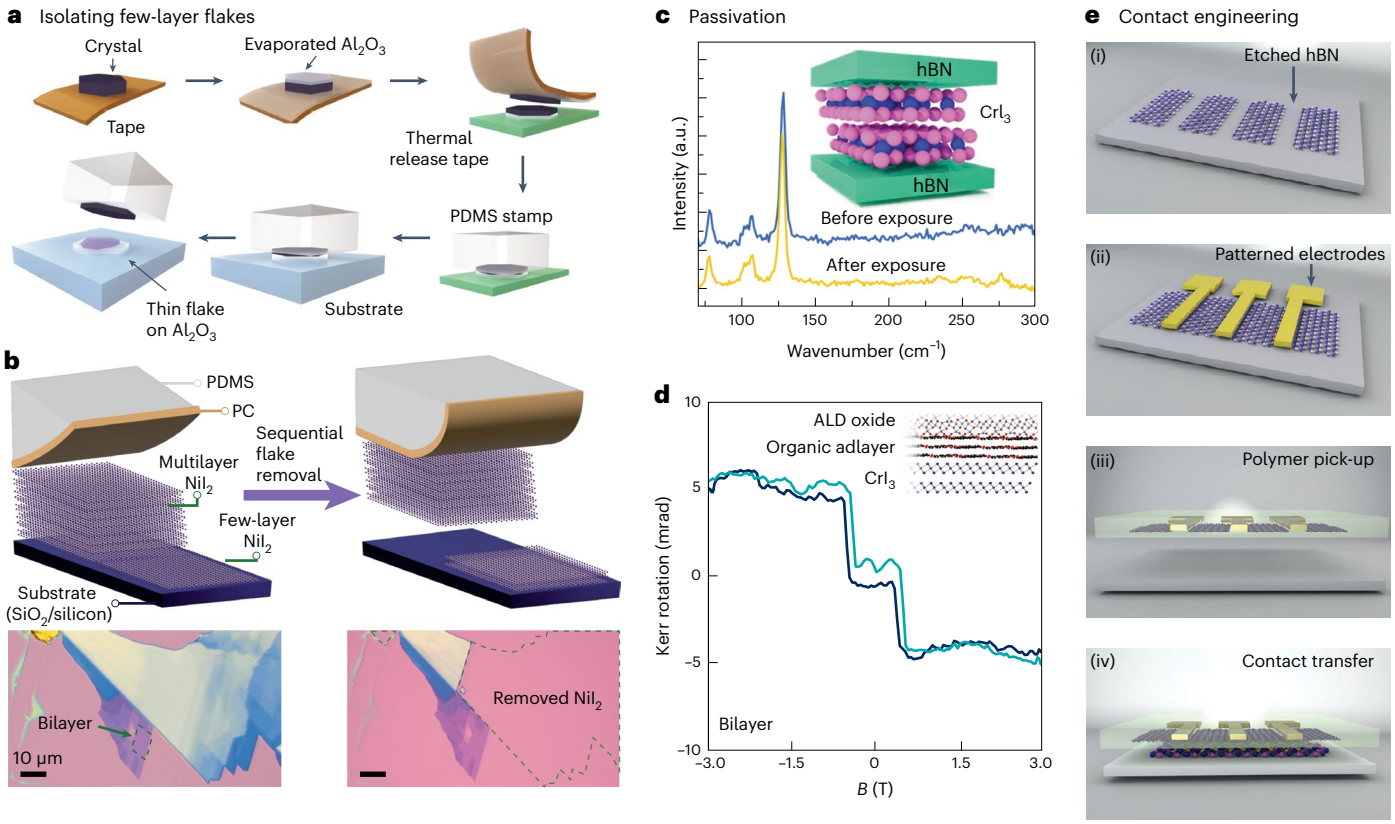

Fig. 4 | Overcoming challenges in fabrication and charge transport characterization for vdW magnets. a, Schematic of the alumina-assisted mechanical exfoliation method. The strong adhesion of the crystal to the evaporated alumina enables exfoliation of few-layer Fe_3GeTe_2 (ref. 49). **b**, Schematic and optical images demonstrating the removal of bulk NiI_2 crystals using polycarbonate/polydimethylsiloxane (PC/PDMS) stamps to isolate few-layer NiI_2 (ref. 51). **c**, Raman spectra of hBN-encapsulated CrI_3 before and after 10 days of ambient conditions with the inset showing a schematic of the heterostructure[56]. **d**, Kerr rotation versus field for ALD-encapsulated bilayer CrI_3. The inset shows a side-view schematic of the CrI_3 bilayer, organic adlayer and ALD oxide with blue and green corresponding to the forward and reverse sweeps of the magnetic field, respectively[57]. **e**, Metal contact transfer scheme using etched hBN and patterned electrodes onto a vdW flake[64]. Panels adapted with permission from: **a**, ref. 49, Springer Nature Ltd; **b**, ref. 51, Wiley; **c**, ref. 56, American Chemical Society; **d**, ref. 57, American Chemical Society; **e**, ref. 64, Springer Nature Ltd.

probing of the AFM phase transition, where the conductance shows a peak due to reduced spin fluctuation scattering[54]. The ambient stability of CrSBr has also facilitated the fabrication of multi-terminal devices using traditional lithography, thus revealing highly anisotropic quasi-one-dimensional transport[53].

Other gate-tunable vdW magnetic semiconductors (such as $CrGeTe_3$ and NiI_2) require additional precautions to achieve measurable charge transport at low temperatures owing to their chemical instability. In these cases, FET fabrication requires vdW materials for all components (such as graphene contacts and hBN dielectric layers) to minimize interfacial chemical reactions, followed by the encapsulation of the entire device stack to prevent ambient degradation. For example, the fabrication of air-stable, multi-terminal devices using an all vdW stack, in conjunction with selective etching and conformal growth of ALD alumina, has enabled magnetoresistance measurements down to 2 K in NiI_2 (ref. 51). All vdW devices using hBN as the dielectric layers has the additional benefit of reducing interfacial charge carrier scattering compared with conventional dielectrics such as SiO_2. In this manner, although few-layer FETs using $CrGeTe_3$ in contact with a SiO_2 dielectric are insulating below 150 K, the incorporation of $CrGeTe_3$ into all vdW devices results in gate-tunable charge transport down to cryogenic temperatures with an on/off current ratio I_{ON}/I_{OFF} approaching 10^3 (ref. 63). While graphene minimizes contact resistance with vdW semiconductors and is preferred over bulk metallic contacts for the most chemically reactive materials (such as NiI_2 and $CrGeTe_3$)[63], some device applications require metallic contacts such as high/low work function metals for facilitating the injection of holes/electrons based on band alignment, FM metals for spin injection and high-atomic-number metals for strong spin–orbit coupling (such as Pt). To avoid interfacial degradation induced by metal evaporation, it is possible to dry transfer these metallic contacts using pre-patterned hBN[64–66]. The resulting transferred metallic vdW contacts avoid metallization at the semiconductor/metal interface and leads to a low contact resistance and reduced Fermi-level pinning[64].

Although hBN is the most commonly used dielectric in vdW devices, its relatively low dielectric constant means that alternative high-κ dielectrics are needed in devices that require strong electrostatic gating. For example, HfO_2 provides a high dielectric constant (κ) of around 13–17 (ref. 67), which can be grown on vdW materials using seeded ALD[59]. Alternatively, strontium titanium oxide thin films (κ of around 17–20) can be dry-transferred, enabling a large I_{ON}/I_{OFF} of around 10^8 and a low subthreshold swing of around 66 mV per decade for MoS_2 (ref. 68). Electrostatic gating using ionic liquids is another method for enhancing capacitive coupling. In this case, the electric double layer increases the gate capacitance up to a few microfarad per square centimetre, which results in high charge carrier density modulation at low applied voltages, ultimately enabling charge transport in $CrGeTe_3$ at temperatures as low as 20 K (ref. 63).

Advantages and challenges

Opto-spintronic devices formed from vdW materials have several advantages compared with those formed from their bulk counterparts.

https://doi.org/10.1038/s41928-024-01167-3

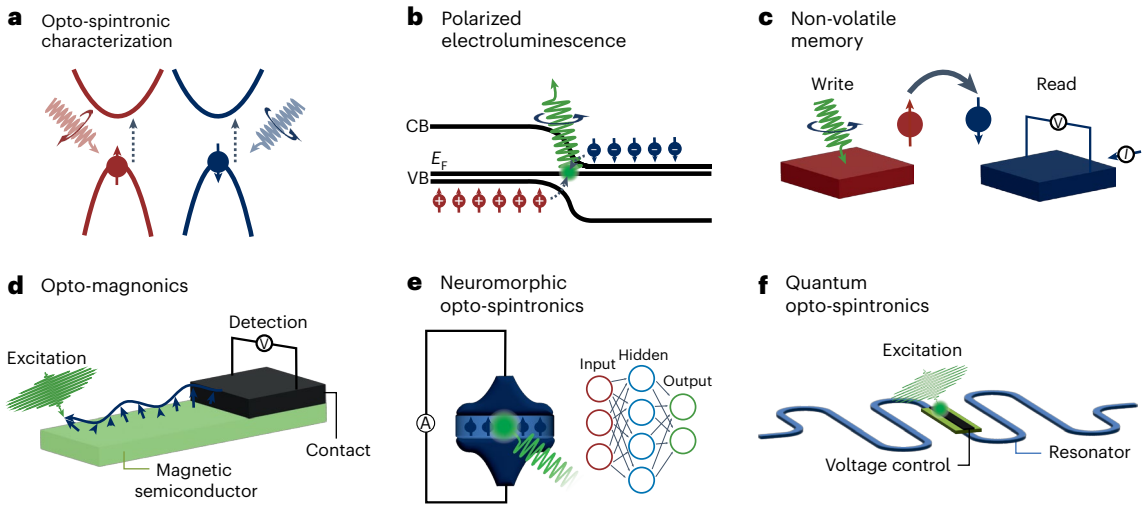

Fig. 5 | Opto-spintronic device applications based on vdW semiconductors. **a**, A schematic illustrating spin-polarized bands that provide a means of characterization using photocurrent and photovoltage spectroscopy. **b**, Polarized electroluminescence based on a p–n heterojunction between two magnetic semiconductors. CB, VB and E_F indicate the conduction band, valence band and Fermi level, respectively. **c**, Opto-spintronic non-volatile memory utilizing optical writing and electrical readout. **d**, Opto-magnonics utilizing optical initialization of spin waves and electrical detection. **e**, Opto-spintronics for neuromorphic computing hardware using spin-based artificial synapses. **f**, Quantum opto-spintronics for quantum transduction utilizing magnon coupling.

However, a direct comparison between device metrics of bulk and vdW devices is challenging due to limited prototypes and a lack of standardized benchmarking. Nevertheless, published proof-of-concept vdW spintronic devices can inform their potential advantages over corresponding devices fabricated from bulk materials. For example, bulk magnetic semiconductors systems are typically fabricated through doping semiconductors with magnetic ions to form semiconducting alloys known as dilute magnetic semiconductors. The random distribution of magnetic atoms in the lattice results in increased scattering sites for electronic carriers, which results in lower mobility, typically on the order of 1–10 $cm^2 V^{-1} s^{-1}$ (refs. 69–71). So far, identified vdW magnetic semiconductors have reported similar mobility values, with that of NiI_2 (1 $cm^2 V^{-1} s^{-1}$) among the largest[51]. While the largest magnetoresistance in dilute magnetic semiconductors is around 70% (ref. 72), an order of magnitude larger magnetoresistance ratios are obtained in bulk magnetic tunnelling junctions (with a maximum ratio of around 800% in a CoFeB/MgO/CoFeB heterostructure)[73]. In comparison, a much larger magnetoresistance ratio of around 5,000% has been observed in the vdW magnetic semiconductor $CrPS_4$. In addition, CrI_3 integrated into a vdW magnetic tunnelling junction showed a record-high magnetoresistance in excess of 10,000% (refs. 61,74).

In the context of opto-spintronic applications, vdW materials present additional advantages compared with bulk systems. For instance, the reduced dielectric screening and magneto-electric effects in vdW materials enable electrostatic control of magnetism, which can be exploited in opto-spintronic devices[39,74,75]. Magnetic order can also be tuned externally by strain or electromagnetic radiation in vdW materials, thus presenting opportunities for flexible opto-spintronic applications. Moreover, the layered structure of vdW magnets allows for intercalation with small molecules that can be leveraged to control interlayer magnetic coupling. For example, monolayer behaviour can be obtained by molecular intercalation of multilayer vdW materials, as has been shown for $RuCl_3$ (refs. 76,77).

Heterostructures between vdW magnets and other vdW materials open additional opportunities to control electronic band alignments and magnetic proximity effects[13]. In addition, controlling the relative angle between vdW layers during stacking enables the creation of moiré twisted structures with potential energy modulations larger than the crystal lattice, ultimately providing band-structure engineering. This approach has resulted in the realization of diverse quantum phenomena, including orbital magnetism in twisted bilayer graphene, light-induced ferromagnetism in TMDC heterostructures and moiré magnetism in twisted CrI_3 (ref. 78). Furthermore, moiré superlattices are expected to show a strong photoresponse due to a large number of available states in their flat bands and the emergence of new transitions between the correlated insulating gap and the moiré superlattice bandgap on an energy scale of around 10 meV (terahertz range)[79,80]. As moiré superlattices are typically accompanied by symmetry breaking, these systems lead to additional unique physical phenomena such as the bulk photovoltaic effect demonstrated in twisted bilayer graphene[81].

While the field of vdW opto-spintronics is progressing rapidly, challenges still need to be overcome. Most prominently, semiconducting vdW magnetic materials are almost exclusively prepared using micromechanical exfoliation, which is not scalable. Therefore, concerted effort will be needed to achieve large-area, homogeneous, thickness-controlled growth of semiconducting vdW magnetic materials. Another major challenge is increasing the magnetic-ordering temperatures of semiconducting vdW magnetic materials from their typical cryogenic values up to room temperature. Compositional modulation strategies such as alloying or doping may allow progress in this regard. Finally, opportunities remain for the discovery of additional semiconducting vdW magnetic materials by exploring portions of the periodic table that have been successful for bulk magnetic materials, but have not yet been extensively pursued in the 2D limit. Due to the broad experimental phase space, theoretical efforts will be critical for guiding efficient discovery of future room-temperature 2D magnets[82]. As these remaining challenges are overcome, the full potential of vdW opto-spintronics will be realized for both fundamental science and applied technologies.

Emerging applications

Strong light–matter interactions through magneto-optical effects in addition to excitonic spin–charge coupling can be used for characterizing vdW magnetic materials (such as MOKE). In addition, beyond characterization, electrically conductive spin-polarized vdW materials enable novel device functionalities (Fig. 5). For example, the difference

in preferential absorption of right- or left-circularly polarized light for different magnetizations of 2D CrI_3 has enabled helicity detectors that rely on measuring tunnelling photocurrent[14–16]. Alternatively, photocurrent measurements with polarized light excitation allow probing the magnetic order in low-dimensional materials as a complement to optical methods (such as MOKE, MCD, SHG, LD, PL and Raman spectroscopies)[14–16] or measurements of tunnelling magnetoresistance[60,61] (Fig. 5a). Moreover, spectrally resolved photocurrent measurements allow targeting of specific electronic transitions such as states within the bandgap, excitons or high-energy states in the bands, thus providing an alternative means for probing the correlation between these states and underlying magnetic order. In addition, photocurrent spectroscopy measurements can be used in conjunction with external stimuli such as strain, electric and magnetic fields, and electrostatic doping. In particular, photocurrent measurements of excitonic transitions in CrSBr can be used to further corroborate the effects of external magnetic fields and strain previously observed using PL spectroscopy[44]. Opto-spintronic detection methods also offer the opportunity to probe the effect of external stimuli, such as electrostatic doping, on the many-body excitonic transitions in NiI_2 and $NiPS_3$ (refs. 29,30).

The recombination of excitons coupled with long-range magnetic order often results in polarized luminescence (Fig. 5b). In dilute magnetic semiconductors, polarized electroluminescence is challenging due to poor spin injection from magnetic contacts and the inefficiency of maintaining spin-polarized currents, making polarized LEDs from these materials impractical[83]. In contrast, the benefit of vdW magnetic semiconductors is that external magnetic fields or spin injection from contacts are unnecessary to achieve electrically driven polarized luminescence. Potential methods to realize such LEDs include fabricating p–n junctions using two semiconducting spin-polarized materials. Alternatively, transient-mode electroluminescence can be employed, where a square-wave a.c. voltage between the gate and a grounded semiconducting channel results in the simultaneous presence of injected electrons (holes) and trapped holes (electrons) in the semiconductor, which recombine and luminesce with an intensity determined by gate voltage amplitude and frequency[84]. Another approach to electroluminescence is resonant tunnelling through a graphene/hBN/semiconductor/hBN/graphene stack, which injects electrons and holes through the semiconductor using the two graphene electrodes. Applying a voltage across the stack shifts the Fermi level to reside in the valance band of one graphene electrode and the conduction band of the other[85]. The resonant tunnelling of holes and electrons through the stack thus results in electroluminescence based on excitonic transitions in the semiconductor. For magnetic semiconductors, tuning the drain and gate biases would allow for transitions between specific spin-polarized bands to achieve polarized luminescence. A similar concept was recently realized in a Fe_3GeTe_2/hBN/WSe_2/hBN/graphene tunnelling structure, where injection of spin-polarized holes from ferromagnetic Fe_3GeTe_2 into the non-magnetic semiconductor WSe_2 resulted in helical electroluminescence due to population imbalance in ±K valleys[86].

Writing and reading memory states at ultrafast terahertz frequencies can also be enabled by opto-spintronic devices based on vdW AFM materials (Fig. 5c), making them of particular interest for high-frequency applications through optical writing and electrical readout. The first demonstration of optically writing the magnetic state was performed for metallic FM nickel films with subpicosecond demagnetization using femtosecond laser pulses[87]. In these metallic films, laser pulses heat the sample close to the Curie temperature, and the helicity of the light induces a preferential spin orientation, enabling control of the film magnetization[88]. By contrast, in non-metallic materials, spins have been manipulated by resonantly pumping electronic transitions at terahertz frequencies, inducing a spin orientation coupled with the polarization of light[89,90]. Similar phenomena have been observed in CrI_3, resulting in optical switching of magnetization, which depends on the polarization and wavelength of light (correlated with electronic transitions)[45]. This ultrafast optical spin manipulation enables magnetically written binary states at terahertz frequencies[90].

In addition to optical writing magnetic states, readout is also required, which can be achieved electrically (Fig. 5c). Although the optical writing of A-type AFM CrI_3 reverses the magnetization direction (such as from up to down), tunnelling magnetoresistance is infeasible for readout as it is not sensitive to the magnetization direction[60,61]. Therefore, alternative means of electrical detection have been explored such as proximity effects and interfacial spin polarizations between two vdW materials. For example, the measurable changes in antisymmetric magnetoresistance due to magnetic switching at the AFM/FM interface are sensitive to the spin direction, which allows electrical readout of the magnetic state[91]. Other strategies for electrical readout of magnetic states include the spin Hall effect, inverse spin Hall effect, anisotropic magnetoresistance and the anomalous Hall effect, all of which depend on the magnetic structure and device geometry[92–94]. For these reasons, when designing vdW opto-spintronic devices, it is essential to consider the sample geometry and magnetic structure when identifying the optimal means of electrically detecting changes in magnetic states.

Magnonic devices carry information via spin waves (magnons) instead of charge carriers[95], which present some advantages (such as potentially higher speed) compared with conventional electronic devices (Fig. 5d). In particular, optically excited magnons via stimulated Raman scattering are sensitive to light polarization and energy, enabling manipulation of the amplitude and phase at ultrafast timescales[96]. Semiconducting 2D magnets with strong spin–charge coupling are ideal candidates for magnonic devices as the optical excitation of coherent magnons are correlated with electronic transitions[35,36]. The electrical detection of magnons often makes use of a non-local geometry (measuring voltage difference at a distance from current flow) such as inverse spin Hall effect detection via a strong spin–orbit coupling metal (such as Pt). In this case, the optical generation of magnons produces pure spin currents, which are detectable in Pt due to strong spin–orbit coupling[36,97,98]. This non-local geometry can detect spin waves for up to several micrometres as has been demonstrated in $MnPS_3$ (ref. 99). As patterning Pt contacts may not be feasible for some chemically reactive vdW magnetic materials, an alternative approach would be to transfer Pt/hBN contacts, which has been demonstrated for other semiconducting materials[64].

The strong spin–charge coupling in many 2D magnetic semiconductors presents additional opportunities to optically excite magnons correlated with the semiconducting band structure, which can be tuned by external stimuli. For example, the frequencies of the magnons in CrI_3 can be manipulated through electrostatic doping[100]. Alternatively, external magnetic fields in conjunction with optically launched phonons can hybridize the phonon and magnon branches, modulating their frequencies[35,101]. Moreover, A-type AFM materials (such as CrI_3, CrSBr) offer the high speed that is intrinsic to AFM materials and are sensitive to external magnetic fields, which can modulate the magnetization between FM and AFM and, consequently, manipulate the magnon modes[33,36]. Electrically detectable and optically excited coherent spin waves that are sensitive to frequency, amplitude and phase modulation via external stimuli can be used in low-power memory applications and magnonic logic circuits[102,103].

Among next-generation computing systems, neuromorphic computing hardware aims to eliminate the disparity between bio-realistic neural network algorithms and energy-consuming logic operations in complementary metal–oxide–semiconductor circuits. Synaptic connections have a central role in emerging neuromorphic hardware, which are realized by analogue non-volatile memory that can be written and read in a highly parallelized manner from an artificial neural network. Among the leading candidates for non-volatile memories, spintronic memory is particularly attractive due to inherent low-energy operation in spin-based devices (Fig. 5e). In addition to synaptic memory,

spin-based switches have nonlinear dynamics to mimic bio-realistic neurons or activation functions to realize asynchronous spiking neural networks[104]. The unique optoelectronic properties of 2D magnetic semiconductors hold potential for neuromorphic hardware due to the combination of low-energy magnetic switching and parallelized read/write operations in photonic systems[105]. While linear optical training of neural network synapses is an advantage for many conventional artificial intelligence algorithms, nonlinear activation functions are increasingly being explored for more bio-realistic machine learning, which can be realized either by a photodetector or by magnetic switching in 2D magnetic materials and heterojunctions[106].

Heterojunctions composed of vdW magnets and other monolayers such as graphene and TMDCs are further broadening the scope of opto-spintronic devices that can be leveraged for neuromorphic computing[8,107]. For example, vertical graphene/CrI_3/graphene heterojunctions have shown memristive switching where the switching voltage can be controlled by applied magnetic fields[108]. In addition, stochastic switching and domain-wall motion in bulk ferromagnetic materials have been exploited in probabilistic networks for integer factorization and chaotic circuits, respectively[109,110]. Monolayer magnetic materials host not only tunable domain-wall motion but also other attributes, such as dual gating and coupled state variables in opto-spintronic devices, which can be exploited for bio-realistic neuromorphic hardware[111]. Furthermore, spatially inhomogeneous exchange interactions in AFMs allow multi-level analogue memory for artificial synapses and provide a unique platform for reservoir computing. In this context, skyrmionic and straintronic devices based on vdW materials have added benefits resulting from stimuli-dependent tunability[112].

Quantum information science is another next-generation computing paradigm that combines aspects of fundamental quantum physics with information theory. Integrating different quantum modules, such as materials engineering, circuit design and dynamic operation, benefits from hybrid systems, providing tunability and flexibility[113]. These hybrid systems are often based on magnonics, where magnons are used for quantum transduction via the realization of different types of magnon coupling such as magnon–photon coupling[114,115]. Recently, strong coupling between microwave photons and nano-permalloy was realized on-chip using superconducting thin-film resonators[116,117]. This strong coupling opens opportunities for the development of high-speed coherent transducers for on-chip coherent information transfer. Various types of magnon coupling have been observed in 2D magnetic semiconductors, including magnon–magnon scattering in $CrCl_3$ (ref. 118), phonon–magnon coupling in $FePS_3$ (ref. 35) and exciton–magnon coupling in CrSBr (refs. 36,37). These forms of magnon coupling present opportunities for 2D magnets in quantum transduction applications including on-chip coupling with superconducting resonators. In contrast to permalloy nanomagnets, the magnetic properties and magnon modes of 2D magnets can be tuned via strain, optical or spintronic effects, such as spin torque or voltage-controlled magnetic anisotropy[37,47] (Fig. 5f). Control over the magnon modes in 2D magnets will further allow the realization of tunable coupling between the quantum resonator and the 2D magnet, thus enabling the development of increasingly sophisticated quantum information systems.

Outlook

Light–matter interactions in 2D magnetic semiconducting materials are central to the future design and fabrication of opto-spintronic devices. Understanding the chemical reactivity of these vdW magnetic semiconductors, in addition to developing robust passivation and encapsulation schemes, is critical to preserving their pristine physical properties and allowing reliable studies of spin- and charge-based phenomena. The sensitivity of the materials to electric fields, strain, carrier density and optical manipulation provides a means to manipulate magnetization and related properties. Moreover, the strong interplay between optoelectronic and magnetic degrees of freedom is key to device applications such as electric-field control of magnetism, high-frequency devices and ultralow power memory[119]. The sensitivity of semiconducting vdW magnets to light–matter interactions and gate modulation also provides opportunities to develop opto-spintronic devices for non-volatile memory, neuromorphic computing, magnonics and quantum transduction applications.

References

1. Baibich, M. N. et al. Giant magnetoresistance of (001)Fe/(001)Cr magnetic superlattices. *Phys. Rev. Lett.* **61**, 2472–2475 (1988). **Paper on the discovery of giant magnetoresistance**.
2. Binasch, G., Grunberg, P., Saurenbach, F. & Zinn, W. Enhanced magnetoresistance in layered magnetic structures with antiferromagnetic interlayer exchange. *Phys. Rev. B* **39**, 4828–4830 (1989). **Paper on the discovery of giant magnetoresistance**.
3. Dieny, B. et al. Opportunities and challenges for spintronics in the microelectronics industry. *Nat. Electron.* **3**, 446–459 (2020).
4. Novoselov, K. S. et al. Electric field effect in atomically thin carbon films. *Science* **306**, 666–669 (2004).
5. Sangwan, V. K. & Hersam, M. C. Electronic transport in two-dimensional materials. *Annu. Rev. Phys. Chem.* **69**, 299–325 (2018).
6. Gong, C. et al. Discovery of intrinsic ferromagnetism in two-dimensional van der Waals crystals. *Nature* **546**, 265–269 (2017).
7. Huang, B. et al. Layer-dependent ferromagnetism in a van der Waals crystal down to the monolayer limit. *Nature* **546**, 270–273 (2017). **This paper reports 2D magnetism**.
8. Wang, Q. H. et al. The magnetic genome of two-dimensional van der Waals materials. *ACS Nano* **16**, 6960–7079 (2022).
9. Lin, X., Yang, W., Wang, K. L. & Zhao, W. Two-dimensional spintronics for low-power electronics. *Nat. Electron.* **2**, 274–283 (2019).
10. Yang, H. et al. Two-dimensional materials prospects for non-volatile spintronic memories. *Nature* **606**, 663–673 (2022).
11. Dey, P. & Roy, J. N. *Spintronics: Fundamentals and Applications* 163–183 (Springer, 2021).
12. Sierra, J. F. et al. Van der Waals heterostructures for spintronics and opto-spintronics. *Nat. Nanotechnol.* **16**, 856–868 (2021).
13. Zhong, D. et al. Van der Waals engineering of ferromagnetic semiconductor heterostructures for spin and valleytronics. *Sci. Adv.* **3**, e1603113 (2017).
14. Song, T. et al. Spin photovoltaic effect in magnetic van der Waals heterostructures. *Sci. Adv.* **7**, eabg8094 (2021). **This paper reports the spin photovoltaic effect in a vdW heterostructure for light helicity detection**.
15. Cheng, X. et al. Light helicity detector based on 2D magnetic semiconductor CrI_3. *Nat. Commun.* **12**, 6874 (2021). **This paper reports the fabrication of vdW opto-spintronic devices**.
16. Chen, J. et al. Optical helicity and polarization dependent NIR negative photocurrent in the 2D magnetic semiconductor CrI_3. *Adv. Opt. Mater.* **12**, 2301488 (2023).
17. Nemec, P., Fiebig, M., Kampfrath, T. & Kimel, A. V. Antiferromagnetic opto-spintronics. *Nat. Phys.* **14**, 229–241 (2018).
18. Hwangbo, K. et al. Highly anisotropic excitons and multiple phonon bound states in a van der Waals antiferromagnetic insulator. *Nat. Nanotechnol.* **16**, 655–660 (2021).
19. Zhang, Q. et al. Observation of giant optical linear dichroism in a zigzag antiferromagnet $FePS_3$. *Nano Lett.* **21**, 6938–6945 (2021).
20. Sun, Z. et al. Giant nonreciprocal second-harmonic generation from antiferromagnetic bilayer CrI_3. *Nature* **572**, 497–501 (2019).

21. Lee, K. et al. Magnetic order and symmetry in the 2D semiconductor CrSBr. *Nano Lett.* **21**, 3511–3517 (2021).
22. Song, Q. et al. Evidence for a single-layer van der Waals multiferroic. *Nature* **602**, 601–605 (2022).
This paper reports multiferroicity in ultrathin vdW materials.
23. Fumega, A. O. & Lado, J. L. Microscopic origin of multiferroic order in monolayer NiI_2. *2D Mater.* **9**, 025010 (2022).
24. Jin, W. et al. Observation of the polaronic character of excitons in a two-dimensional semiconducting magnet CrI_3. *Nat. Commun.* **11**, 4780 (2020).
25. Seyler, K. L. et al. Ligand-field helical luminescence in a 2D ferromagnetic insulator. *Nat. Phys.* **14**, 277–281 (2018).
26. Grzeszczyk, M. et al. Strongly correlated exciton-magnetization system for optical spin pumping in $CrBr_3$ and CrI_3. *Adv. Mater.* **35**, e2209513 (2023).
27. Wilson, N. P. et al. Interlayer electronic coupling on demand in a 2D magnetic semiconductor. *Nat. Mater.* **20**, 1657–1662 (2021).
28. Wang, Y. et al. Magnetic anisotropy and electric field induced magnetic phase transition in the van der Waals antiferromagnet CrSBr. *Phys. Rev. B* **108**, 054401 (2023).
29. Kang, S. et al. Coherent many-body exciton in van der Waals antiferromagnet $NiPS_3$. *Nature* **583**, 785–789 (2020).
This paper reports ultranarrow photoluminescence from a low-dimensional antiferromagnet.
30. Son, S. et al. Multiferroic-enabled magnetic-excitons in 2D quantum-entangled van der Waals antiferromagnet NiI_2. *Adv. Mater.* **34**, 2109144 (2021).
31. Li, X. et al. Ultrafast spontaneous localization of a Jahn–Teller exciton polaron in two-dimensional semiconducting CrI_3 by symmetry breaking. *Nano Lett.* **22**, 8755–8762 (2022).
32. Ergecen, E. et al. Magnetically brightened dark electron-phonon bound states in a van der Waals antiferromagnet. *Nat. Commun.* **13**, 98 (2022).
33. Jin, W. et al. Raman fingerprint of two terahertz spin wave branches in a two-dimensional honeycomb Ising ferromagnet. *Nat. Commun.* **9**, 5122 (2018).
34. Cenker, J. et al. Direct observation of two-dimensional magnons in atomically thin CrI_3. *Nat. Phys.* **17**, 20–25 (2021).
35. Mertens, F. et al. Ultrafast coherent THz lattice dynamics coupled to spins in the van der Waals antiferromagnet $FePS_3$. *Adv. Mater.* **35**, 2208355 (2022).
36. Bae, Y. J. et al. Exciton-coupled coherent magnons in a 2D semiconductor. *Nature* **609**, 282–286 (2022).
This paper reports efficient coupling between excitons and magnons.
37. Diederich, G. M. et al. Tunable interaction between excitons and hybridized magnons in a layered semiconductor. *Nat. Nanotechnol.* **18**, 23–28 (2022).
38. Jiang, S., Shan, J. & Mak, K. F. Electric-field switching of two-dimensional van der Waals magnets. *Nat. Mater.* **17**, 406–410 (2018).
39. Jiang, S. et al. Controlling magnetism in 2D CrI_3 by electrostatic doping. *Nat. Nanotechnol.* **13**, 549–553 (2018).
40. Verzhbitskiy, I. A. et al. Controlling the magnetic anisotropy in $Cr_2Ge_2Te_6$ by electrostatic gating. *Nat. Electron.* **3**, 460–465 (2020).
41. Bergeron, H., Lebedev, D. & Hersam, M. C. Polymorphism in post-dichalcogenide two-dimensional materials. *Chem. Rev.* **121**, 2713–2775 (2021).
42. Li, T. et al. Pressure-controlled interlayer magnetism in atomically thin CrI_3. *Nat. Mater.* **18**, 1303–1308 (2019).
43. Song, T. et al. Switching 2D magnetic states via pressure tuning of layer stacking. *Nat. Mater.* **18**, 1298–1302 (2019).
44. Cenker, J. et al. Reversible strain-induced magnetic phase transition in a van der Waals magnet. *Nat. Nanotechnol.* **17**, 256–261 (2022).
45. Zhang, P. et al. All-optical switching of magnetization in atomically thin CrI_3. *Nat. Mater.* **21**, 1373–1378 (2022).
This paper reports optical control of a low-dimensional magnet.
46. Padmanabhan, P. et al. Coherent helicity-dependent spin–phonon oscillations in the ferromagnetic van der Waals crystal CrI_3. *Nat. Commun.* **13**, 4473 (2022).
47. Afanasiev, D. et al. Controlling the anisotropy of a van der Waals antiferromagnet with light. *Sci. Adv.* **7**, eabf3096 (2021).
48. Belvin, C. A. et al. Exciton-driven antiferromagnetic metal in a correlated van der Waals insulator. *Nat. Commun.* **12**, 4837 (2021).
49. Deng, Y. et al. Gate-tunable room-temperature ferromagnetism in two-dimensional Fe_3GeTe_2. *Nature* **563**, 94–99 (2018).
50. Huang, Y. et al. Universal mechanical exfoliation of large-area 2D crystals. *Nat. Commun.* **11**, 2453 (2020).
51. Lebedev, D. et al. Electrical interrogation of thickness-dependent multiferroic phase transitions in the 2D antiferromagnetic semiconductor NiI_2. *Adv. Funct. Mat.* **33**, 2212568 (2023).
52. Telford, E. J. et al. Layered antiferromagnetism induces large negative magnetoresistance in the van der Waals semiconductor CrSBr. *Adv. Mater.* **32**, e2003240 (2020).
53. Wu, F. et al. Quasi-1D electronic transport in a 2D magnetic semiconductor. *Adv. Mater.* **34**, e2109759 (2022).
54. Telford, E. J. et al. Coupling between magnetic order and charge transport in a two-dimensional magnetic semiconductor. *Nat. Mater.* **21**, 754–760 (2022).
55. Kuo, C. T. et al. Exfoliation and Raman spectroscopic fingerprint of few-layer $NiPS_3$ van der Waals crystals. *Sci. Rep.* **6**, 20904 (2016).
56. Shcherbakov, D. et al. Raman spectroscopy, photocatalytic degradation, and stabilization of atomically thin chromium tri-iodide. *Nano Lett.* **18**, 4214–4219 (2018).
57. Gish, J. T. et al. Ambient-stable two-dimensional CrI_3 via organic-inorganic encapsulation. *ACS Nano* **15**, 10659–10667 (2021).
58. Wells, S. A. et al. Suppressing ambient degradation of exfoliated inse nanosheet devices via seeded atomic layer deposition encapsulation. *Nano Lett.* **18**, 7876–7882 (2018).
59. Alaboson, J. M. P. et al. Seeding atomic layer deposition of high-*k* dielectrics on epitaxial graphene with organic self-assembled monolayers. *ACS Nano* **5**, 5223–5232 (2011).
60. Wang, Z. et al. Very large tunneling magnetoresistance in layered magnetic semiconductor CrI_3. *Nat. Commun.* **9**, 2516 (2018).
61. Song, T. et al. Giant tunneling magnetoresistance in spin-filter van der Waals heterostructures. *Science* **360**, 1214–1218 (2018).
62. Jiang, S. et al. Spin tunnel field-effect transistors based on two-dimensional van der Waals heterostructures. *Nat. Electron.* **2**, 159–163 (2019).
63. Wang, Z. et al. Electric-field control of magnetism in a few-layered van der Waals ferromagnetic semiconductor. *Nat. Nanotechnol.* **13**, 554–559 (2018).
64. Liu, Y. et al. Low-resistance metal contacts to encapsulated semiconductor monolayers with long transfer length. *Nat. Electron.* **5**, 579–585 (2022).
65. Liu, L. et al. Transferred van der Waals metal electrodes for sub-1-nm MoS_2 vertical transistors. *Nat. Electron.* **4**, 342–347 (2021).
66. Liu, Y. et al. Approaching the Schottky–Mott limit in van der Waals metal-semiconductor junctions. *Nature* **557**, 696–700 (2018).
This paper reports improved device performance using transferred contacts.
67. Li, W. et al. Uniform and ultrathin high-*κ* gate dielectrics for two-dimensional electronic devices. *Nat. Electron.* **2**, 563–571 (2019).
68. Yang, A. J. et al. Van der Waals integration of high-*κ* perovskite oxides and two-dimensional semiconductors. *Nat. Electron.* **5**, 233–240 (2022).

69. Saito, H. et al. Magnetic and transport properties of III–V diluted magnetic semiconductor $Ga_{1x}Cr_xAs$. *J. Appl. Phys.* **89**, 7392–7394 (2001).
70. Ou, S. L., Liu, H. R., Wang, S. Y. & Wuu, D. S. Co-doped ZnO dilute magnetic semiconductor thin films by pulsed laser deposition: excellent transmittance, low resistivity and high mobility. *J. Alloy. Compd.* **663**, 107–115 (2016).
71. Hayashi, T., Tanaka, M., Nishinaga, T. & Shimada, H. Magnetic and magnetotransport properties of new III–V diluted magnetic semiconductors: GaMnAs. *J. Appl. Phys.* **81**, 4865–4867 (1997).
72. Yang, X. et al. K and Mn co-doped $BaCd_2As_2$: a hexagonal structured bulk diluted magnetic semiconductor with large magnetoresistance. *J. Appl. Phys.* **114**, 223905 (2013).
73. Hayakawa, J. et al. Effect of high annealing temperature on giant tunnel magnetoresistance ratio of CoFeB/MgO/CoFeB magnetic tunnel junctions. *Appl. Phys. Lett.* **89**, 232510 (2006).
74. Wu, F. et al. Gate-controlled magnetotransport and electrostatic modulation of magnetism in 2D magnetic semiconductor $CrPS_4$. *Adv. Mater.* **35**, e2211653 (2023).
75. Huang, B. et al. Electrical control of 2D magnetism in bilayer CrI_3. *Nat. Nanotechnol.* **13**, 544–548 (2018).
76. Wang, C. et al. Monolayer atomic crystal molecular superlattices. *Nature* **555**, 231–236 (2018).
77. Lam, D. et al. Liquid-phase exfoliation of magnetically and optoelectronically active ruthenium trichloride nanosheets. *ACS Nano* **16**, 11315–11324 (2022).
78. Du, L. et al. Moire photonics and optoelectronics. *Science* **379**, eadg0014 (2023).
79. Deng, B. C. et al. Strong mid-infrared photoresponse in small-twist-angle bilayer graphene. *Nat. Photon.* **14**, 549–553 (2020).
80. Yang, J. et al. Spectroscopy signatures of electron correlations in a trilayer graphene/hBN moire superlattice. *Science* **375**, 1295–1299 (2022).
81. Ma, C. et al. Intelligent infrared sensing enabled by tunable moire quantum geometry. *Nature* **604**, 266–272 (2022).
82. Han, R., Jiang, Z. & Yan, Y. Prediction of novel 2D intrinsic ferromagnetic materials with high Curie temperature and large perpendicular magnetic anisotropy. *J. Phys. Chem. C* **124**, 7956–7964 (2020).
83. Fiederling, R. et al. Injection and detection of a spin-polarized current in a light-emitting diode. *Nature* **402**, 787–790 (1999).
84. Lien, D. H. et al. Large-area and bright pulsed electroluminescence in monolayer semiconductors. *Nat. Commun.* **9**, 1229 (2018).
85. Zultak, J. et al. Ultra-thin van der Waals crystals as semiconductor quantum wells. *Nat. Commun.* **11**, 125 (2020).
86. Li, J. X. et al. Electric control of valley polarization in monolayer WSe_2 using a van der Waals magnet. *Nat. Nanotechnol.* **17**, 721–728 (2022).
87. Beaurepaire, E., Merle, J., Daunois, A. & Bigot, J. Ultrafast spin dynamics in ferromagnetic nickel. *Phys. Rev. Lett.* **76**, 4250–4253 (1996).
88. Stanciu, C. D. et al. All-optical magnetic recording with circularly polarized light. *Phys. Rev. Lett.* **99**, 047601 (2007).
89. Baierl, S. et al. Nonlinear spin control by terahertz-driven anisotropy fields. *Nat. Photon.* **10**, 715–718 (2016).
90. Stupakiewicz, A. et al. Ultrafast nonthermal photo-magnetic recording in a transparent medium. *Nature* **542**, 71–74 (2017).
91. Hu, G. et al. Antisymmetric magnetoresistance in a van der Waals antiferromagnetic/ferromagnetic layered $MnPS_3$/Fe_3GeTe_2 stacking heterostructure. *ACS Nano* **14**, 12037–12044 (2020).
92. Chen, X. et al. Observation of the antiferromagnetic spin Hall effect. *Nat. Mater.* **20**, 800–804 (2021).
93. Wang, X. R. Anomalous spin Hall and inverse spin Hall effects in magnetic systems. *Commun. Phys.* **4**, 55 (2021).
94. Kriegner, D. et al. Multiple-stable anisotropic magnetoresistance memory in antiferromagnetic MnTe. *Nat. Commun.* **7**, 11623 (2016).
95. Chumak, A. V., Serga, A. A. & Hillebrands, B. Magnonic crystals for data processing. *J. Phys. D* **50**, 244001 (2017).
96. Bossini, D. et al. Macrospin dynamics in antiferromagnets triggered by sub-20 femtosecond injection of nanomagnons. *Nat. Commun.* **7**, 10645 (2016).
97. Wei, X. Y. et al. Giant magnon spin conductivity in ultrathin yttrium iron garnet films. *Nat. Mater.* **21**, 1352–1356 (2022).
98. Cornelissen, L. J. et al. Long-distance transport of magnon spin information in a magnetic insulator at room temperature. *Nat. Phys.* **11**, 1022–1026 (2015).
99. Xing, W. et al. Magnon transport in quasi-two-dimensional van der Waals antiferromagnets. *Phys. Rev. X* **9**, 011026 (2019).
100. Zhang, X. X. et al. Gate-tunable spin waves in antiferromagnetic atomic bilayers. *Nat. Mater.* **19**, 838–842 (2020).
101. Vaclavkova, D. et al. Magnon polarons in the van der Waals antiferromagnet $FePS_3$. *Phys. Rev. B* **104**, 134437 (2021).
102. Wang, Q. et al. A magnonic directional coupler for integrated magnonic half-adders. *Nat. Electron.* **3**, 765–774 (2020).
103. Wang, Q. et al. A nonlinear magnonic nano-ring resonator. *npj Comput. Mater.* **7**, 192 (2021).
104. Kurenkov, A., Fukami, S. & Ohno, H. Neuromorphic computing with antiferromagnetic spintronics. *J. Appl. Phys.* **128**, 010902 (2020).
105. Shainline, J. M. Optoelectronic intelligence. *Appl. Phys. Lett.* **118**, 160501 (2021).
106. Feng, X., Liu, X. & Ang, K.-W. 2D photonic memristor beyond graphene: progress and prospects. *Nanophotonics* **9**, 1579–1599 (2020).
107. Dayen, J.-F. et al. Two-dimensional van der Waals spinterfaces and magnetic-interfaces. *Appl. Phys. Rev.* **7**, 011303 (2020).
108. Kim, H. H. et al. Magneto-memristive switching in a 2D layer antiferromagnet. *Adv. Mater.* **32**, e1905433 (2020).
109. Borders, W. A. et al. Integer factorization using stochastic magnetic tunnel junctions. *Nature* **573**, 390–393 (2019).
110. Ababei, R. V. et al. Neuromorphic computation with a single magnetic domain wall. *Sci. Rep.* **11**, 15587 (2021).
111. Sangwan, V. K., Liu, S. E., Trivedi, A. R. & Hersam, M. C. Two-dimensional materials for bio-realistic neuronal computing networks. *Matter* **5**, 4133–4152 (2022).
112. Rajib, M. M. et al. Skyrmion based energy-efficient straintronic physical reservoir computing. *Neuromorph. Comput. Eng.* **2**, 044011 (2022).
113. Awschalom, D. D. et al. Quantum engineering with hybrid magnonic systems and materials. *IEEE Trans. Quantum Eng.* **2**, 1–36 (2021).
114. Lachance-Quirion, D. et al. Hybrid quantum systems based on magnonics. *Appl. Phys. Express* **12**, 070101 (2019).
115. Li, Y. et al. Hybrid magnonics: physics, circuits, and applications for coherent information processing. *J. Appl. Phys.* **128**, 130902 (2020).
116. Li, Y. et al. Strong coupling between magnons and microwave photons in on-chip ferromagnet-superconductor thin-film devices. *Phys. Rev. Lett.* **123**, 107701 (2019).
117. Hou, J. T. & Liu, L. Strong coupling between microwave photons and nanomagnet magnons. *Phys. Rev. Lett.* **123**, 107702 (2019).
118. MacNeill, D. et al. Gigahertz frequency antiferromagnetic resonance and strong magnon-magnon coupling in the layered crystal $CrCl_3$. *Phys. Rev. Lett.* **123**, 047204 (2019).
119. Spaldin, N. A. & Ramesh, R. Advances in magnetoelectric multiferroics. *Nat. Mater.* **18**, 203–212 (2019).

Acknowledgements
This research was supported by the National Science Foundation Division of Materials Research (NSF DMR-2004420) and the Department of Energy (DOE DE-SC0019356).

Author contributions
J.T.G., D.L., T.W.S. and V.K.S. performed the literature review and contributed to the initial draft of the paper. M.C.H. oversaw the research and performed the final editing of the paper.

Competing interests
The authors declare no competing interests.

Additional information
Correspondence and requests for materials should be addressed to Mark C. Hersam.

Peer review information *Nature Electronics* thanks Lun Dai, Yinong Zhang and the other, anonymous, reviewer(s) for their contribution to the peer review of this work.